used as a distal ICA protection system in 15 patients, and a Naviballoon system (Kaneka) was used in 1 patient. With the patient under local anesthesia, a guiding catheter was advanced to the affected common CA, and a self-expandable SMART stent (Cordis Endovascular System) was implanted after predilation with a balloon catheter. Postdilation using a larger balloon catheter was used in 5 patients. For prevention of postoperative stroke related to stenting, 81 mg of aspirin and 200 mg of ticlopidine were routinely administered before CAS. Heparin was intravenously administered during and after CAS in all patients. No complications including cerebral ischemia, retinal ischemia, or groin hematoma occurred during peri- and postoperative stenting in any patient. Postoperative diffusion-weighted MR imaging was routinely performed, and no fresh infarctions that might affect the PET data were found in any patient.

Protocol for PET

Positron emission tomography was conducted 3 times: within 1 month before CAS, 1–7 days after CAS (acute stage), and 3–4 months after CAS. Only 8 patients underwent PET scanning 3–4 months postoperatively. A Headtome V (Shimazu) PET system was used to examine the following parameters: CBF_{rest}, OEF, and CBV using $^{15}O_2$-labeled water, $^{15}O_2$-labeled molecular O_2, or $^{15}O_2$-labeled CO, as previously reported.[18] The $CMRO_2$ and the CBF/CBV ratios were also calculated. The CBF/CBV ratio is an index of CPP according to the previous PET analysis of the relationship between CBF, CBV, and the oxygen extraction ratio.[8] Acetazolamide challenge was performed by intravenous administration of 1000 mg acetazolamide, and the percentage change in CBF from the resting state to the acetazolamide challenge state was calculated as follows: $\%\ CBF_{az} = 100 \times (CBF_{az} - CBF_{rest})/CBF_{rest}$.

Positron emission tomography analysis was performed using elliptical regions of interest located at the centrum semiovale level in each cerebral hemisphere.

TABLE 1: Mean values of the parameters before and after CAS

Parameter	Before	Acute Stage	Chronic Stage
ipsilateral side			
CBFrest (ml/100 ml/min)	37.6 ± 7.9	49.0 ± 10.1	39.1 ± 5.9
$\%CBF_{az}$ (%)	39.9 ± 21.5	42.8 ± 17.4	53.6 ± 13.0
CBV (ml/100g)	3.45 ± 0.69	3.48 ± 0.75	3.41 ± 0.53
CPP (min)	11.12 ± 2.26	14.25 ± 1.99	11.82 ± 3.22
OEF	0.44 ± 0.05	0.43 ± 0.06	0.45 ± 0.03
$CMRO_2$ (ml/100 ml/min)	2.62 ± 0.39	2.73 ± 0.37	2.71 ± 0.33
contralateral side			
CBF_{rest} (ml/100 ml/min)	40.5 ± 7.2	48.1 ± 10.1	39.7 ± 6.7
$\%CBF_{az}$ (%)	53.8 ± 15.7	45.5 ± 17.0	53.0 ± 16.1
CBV (ml/100g)	3.63 ± 0.72	3.66 ± 0.66	3.30 ± 0.46
CPP (min)	11.33 ± 1.86	13.34 ± 2.78	12.36 ± 3.14
OEF	0.42 ± 0.04	0.44 ± 0.06	0.44 ± 0.05
$CMRO_2$ (ml/100 ml/min)	2.75 ± 0.39	2.78 ± 0.38	2.69 ± 0.29

These data assessed from the affected side were compared with those for the control side at each stage. Values were statistically analyzed with unpaired t-tests using StatView 5.0 software (SAS Institute). Probability values < 0.05 were considered statistically significant.

Results

Representative Case

A 71-year-old woman developed pulse-synchronous tinnitus in her right ear. Significant coronary artery stenosis requiring bypass surgery was identified, but stenosis originating in the right ICA was also detected after cerebral angiography. The patient was referred to our institu-

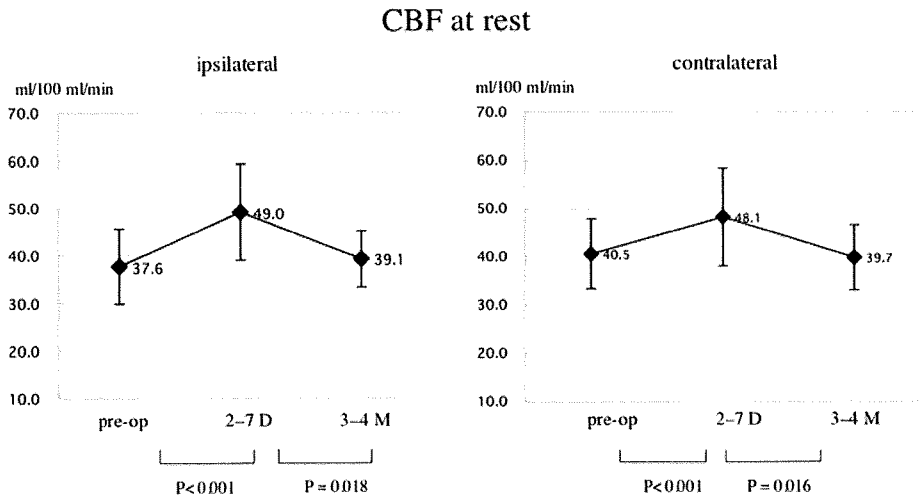

FIG. 3. Graphs showing sequential changes in CBF_{rest} on both sides. Ipsilaterally, significant increases are seen in the postoperative acute stage, with modest increases in the chronic stage. Contralaterally, significant increases are also seen in the acute stage, which reverted to the preoperative level in the chronic stage.

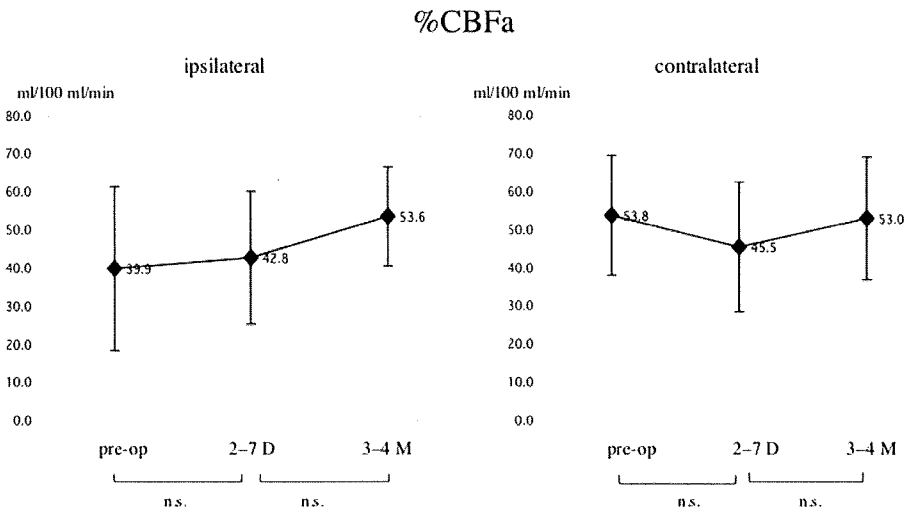

FIG. 4. Graphs showing sequential changes in % CBF_{az}. Mean values initially fell on the affected side but improved over time.

tion for CAS prior to coronary artery bypass. Initial right carotid injection angiography revealed 90% ICA stenosis (Fig. 1A). Angioplasty with a stent was successfully performed with the patient under local anesthesia, and no significant stenosis remained (Fig. 1B). Figure 2 depicts the PET scans and elliptical regions of interest used in this study.

Cerebral Blood Flow

As shown in Table 1, the ipsilateral CBF_{rest} significantly increased in the postoperative acute stage (by a median value of 30.3%) before returning to normal levels 3–4 months postoperatively. The contralateral side also exhibited this trend, increasing by a median of 18.8% in the acute stage (Fig. 3). Statistical analysis revealed significant differences between values measured before and immediately after CAS on both sides. In contrast, the % CBF_{az} on the ipsilateral side displayed gradual improvement, although this change was not significant. On the contralateral side, the % CBF_{az} decreased in the immediate postoperative period compared to pre-CAS levels and then returned to the pre-CAS level by 3–4 months (Fig. 4). Relative to the preoperative state, the CBV was slightly higher immediately after CAS and slightly lower at 3–4 months postoperatively (Fig. 5). The CPP increased rapidly during the acute stage and was found to have decreased on both sides at 3–4 months (Fig. 6); statistical analysis revealed significant differences between the values measured before and just after CAS on both sides.

Oxygen Extraction Fraction and $CMRO_2$

The OEF on the ipsilateral side decreased slightly during the acute stage and then normalized by the 3- to 4-month assessment. Contralateral OEF increased in the acute stage after CAS and remained elevated in the long term, although the changes were minimal (Fig. 7). The ip-

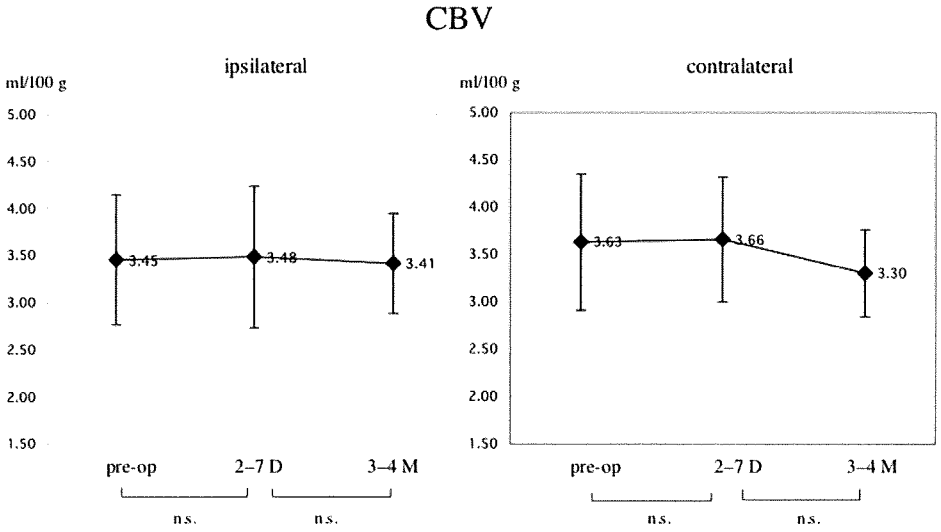

FIG. 5. Graphs showing sequential changes in CBV. Ipsilateral mean values were slightly higher in the acute stage than preoperatively, but decreased in the chronic stage.

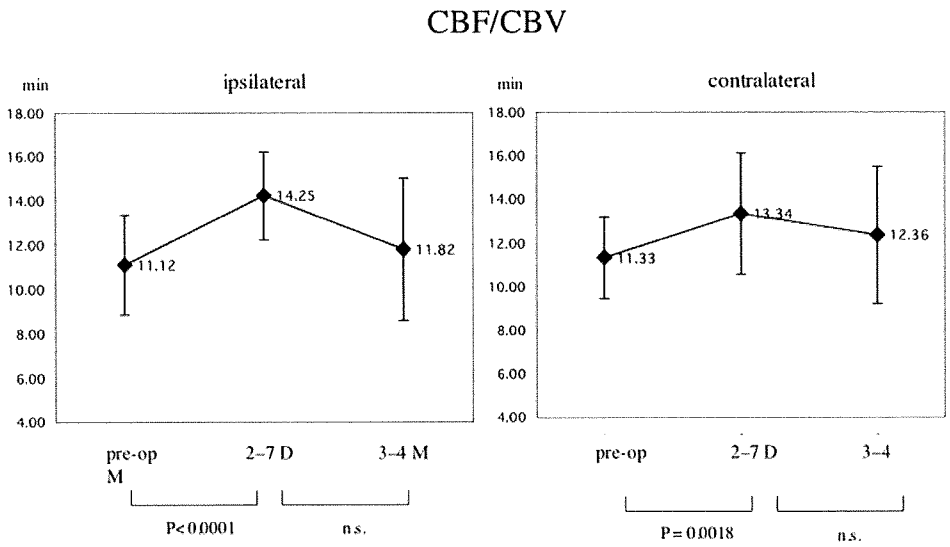

FIG. 6. Graphs showing sequential changes in CPP. Both the ipsilateral and contralateral mean CPP increased significantly in the acute stage but increased only modestly in the chronic stage.

silateral $CMRO_2$ increased slightly immediately after CAS and remained elevated at the 3- to 4-month visit, although this increase was not statistically significant (Fig. 8).

The ratio of ipsilateral to contralateral values (asymmetry index) for CBF_{rest}, % CBF_{az}, CBV, OEF, and $CMRO_2$ tended to approach 1.0 over time (Fig. 9). We noted that % CBF_{az} displayed gradual improvement, whereas CBF_{rest} increased rapidly in the postoperative acute stage before returning to normal levels by 3–4 months postoperatively. In contrast, the OEF temporarily decreased in the acute stage before normalizing over the long term. Ipsilateral values of CBF_{rest} and $CMRO_2$ exceeded contralateral values in the acute stage.

Discussion

Improvements in Cerebral Circulation

The CBF_{rest} was slightly higher at 3–4 months after CAS than it had been preoperatively. In particular, a significant increase in CBF_{rest} of ~ 30% was observed during the acute stage, demonstrating that CAS improves cerebral circulation. This rapid increase in blood flow during the acute stage diminished over time due to arteriolar self-regulation to maintain constant cerebral perfusion and resistance. The CBF at 3–4 months postoperatively was stable and slightly higher than preoperative values. The same trend was seen on the contralateral side, where an increase of 18.8% was seen in the acute stage compared to preoperative values. This increase is thought to reflect blood flow from the collateral circulation via the anterior communicating artery or leptomeningeal anastomosis. Contralaterally, increased CBF immediately after surgery has previously been confirmed by SPECT studies after CEA.[15]

Vascular Reserve

In terms of % CBF_{az}, no significant difference existed

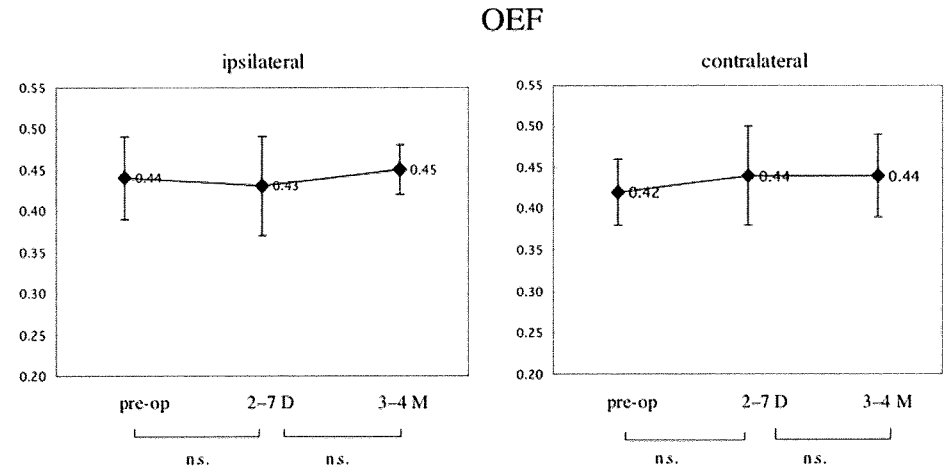

FIG. 7. Graphs showing sequential changes in OEF. The mean OEF did not significantly change at each stage.

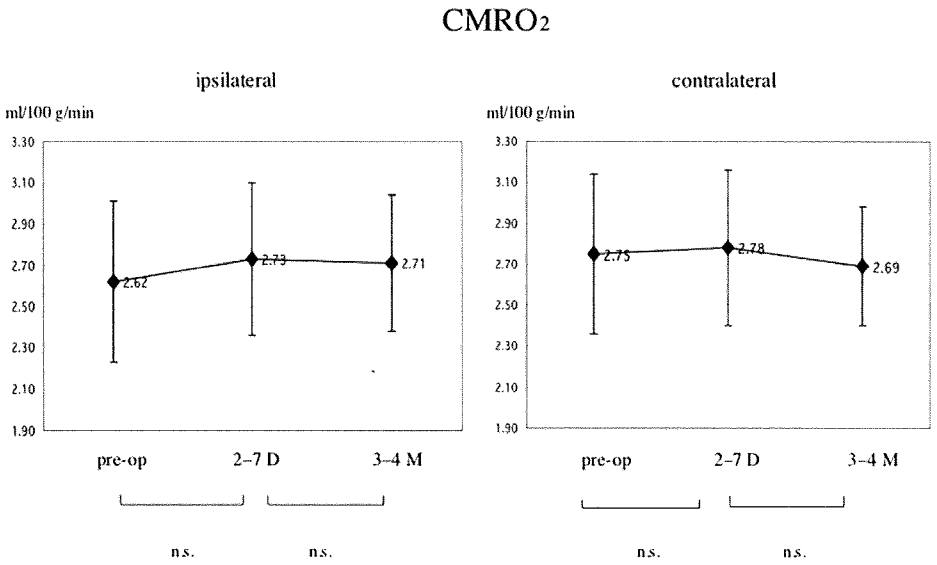

FIG. 8. Graphs showing sequential changes in $CMRO_2$. A tendency toward small increases in ipsilateral $CMRO_2$ was seen in both acute and chronic stages, although no significance differences were noted.

because of marked variations, but some improvements were seen ipsilaterally. Ours is the first study to use PET to demonstrate that stenting improves vascular reactions. On the ipsilateral site, the % CBF_{az} varied preoperatively (39.9 ± 21.5%) but increased with concomitant reductions in variation to 42.8 ± 17.4% in the acute, and 53.6 ± 13.0% at 3–4 months postoperatively. This improvement was marked, showing the greatest degree of improvement compared to the other parameters. In the present study, preoperative cerebrovascular reactivity to acetazolomide in many patients was relatively well maintained at an average of 39.9%; this suggests that marked improvement can be expected in patients with misery perfusion.

Cerebral Blood Volume

Cerebral blood volume is closely related to arteriolar dilation, and increases if vascular stenosis causes decreases in perfusion pressure. Recently Martin et al.[23] performed perfusion MR imaging before and immediately after CAS to assess changes in cerebral circulation; they reported that although there was a small bilateral increase in regional CBV (6%) after stent placement, this was much smaller than the variability observed between 2 different measurements (20%). Wilkinson and associates[35] also documented no significant differences or changes in regional CBV evaluated on perfusion MR imaging between hemispheres before and within 3 hours of

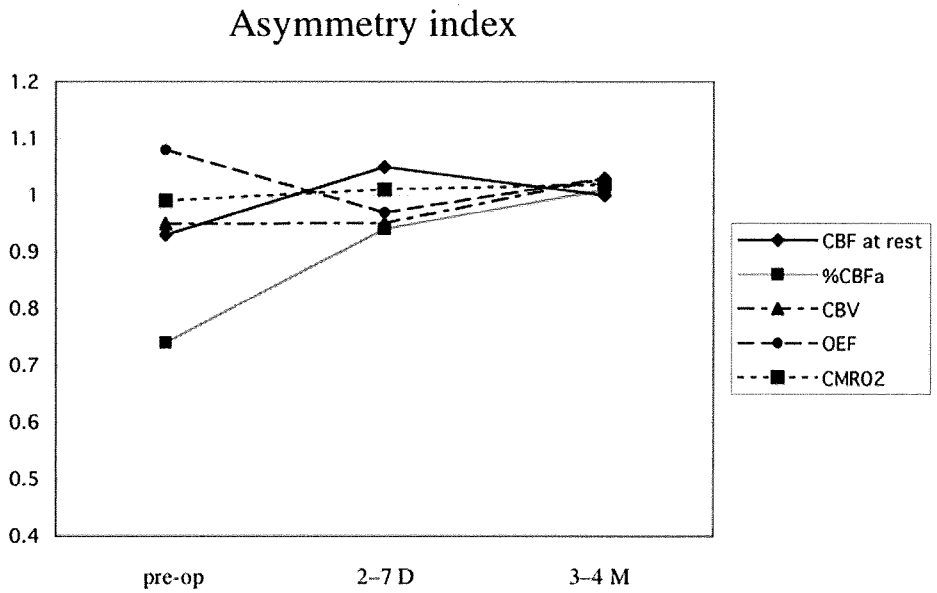

FIG. 9. Graph of asymmetry index. Indices for all parameters approached 1.0 over time. Note that the index for % CBF_{az} increased with time, while the index for CBF_{rest} temporarily exceeded 1.0 in the postoperative acute stage.

CAS. In the present study, CBV increased slightly immediately after surgery and was slightly lower at 3–4 months than it had been preoperatively; this finding did not reach statistical significance. During the acute stage the CBV did not decrease even though the perfusion pressure increased; this finding might be attributable to the arterioles not contracting immediately after surgery. Although Hosoda et al.[15] did not measure CBV, based on SPECT data obtained before and after CEA, these authors noted that abrupt restoration of CPP immediately after surgical correction of a tight ICA stenosis cannot be compensated for by vasoconstriction. However the arterioles presumably contracted to normal size over the long term, thus lowering the CBV.

Cerebral Metabolism

On the ipsilateral side, $CMRO_2$ increased after CAS, albeit insignificantly. This tendency was especially pronounced in the acute stage. Hence, rapid reperfusion to a cerebrum that has been in a state of chronic ischemia may act via some mechanism to increase oxygen metabolism. Marchal and colleagues[21,22] used PET scanning to analyze the hyperperfused regions in 10 patients with cerebral infarctions. Compared to the healthy side, CBF and CBV increased, OEF decreased, and $CMRO_2$ increased moderately. This postischemic oxygen hypermetabolism could involve the following mechanisms: 1) overexcitation of cellular metabolism (such as specific protein synthesis, oxidative phosphorylation, adenosine triphophate formation, synthesis of transcription factors, or growth factors) in cells destined to survive; or 2) excessive firing of neurons undergoing irreversible damage from a massive release of excitatory amino acids during the period of ischemia or early noxious inflammatory processes.[30,32] Consistent with this hypothesis, Heiss et al.[11] used PET in 5 patients with acute stroke, reported an increased ^{11}C-aminoacid (L-methionine) uptake in penumbral tissue surrounding the infarction and experiencing reversible ischemia. In the patients in the present study, stenting was performed for various degrees of cerebral ischemia to restore CBF; hyperemia (hyperperfusion) existed to varying degrees in the acute stage. The changes we observed in the 4 parameters (CBF, CBV, OEF, and $CMRO_2$) before and immediately after CAS matched Marchal and colleagues' findings. Based on our PET results, the state immediately after CAS could resemble hyperperfusion. However Marchal et al. described a hypermetabolic state in the ischemic region of the brain while we identified a hyperperfusion-like phenomenon in a nonischemic region of a brain with asymptomatic CA stenosis, so the parallel may not be exact. We assume, however, that patients with restlessness or headaches after CAS may not only have an increased CBF, but a significantly increased $CMRO_2$. Accumulated data are needed to investigate this issue further.

We saw no significant changes in OEF in our patients, but different results might be obtained in patients with misery perfusion. Unlike in ICA occlusion, the number of misery perfusion cases in which the OEF is ≥ 0.53 should be low in ICA stenosis. Cerebral circulation is assessed on SPECT in patients with misery perfusion because CAS is generally performed soon after onset. As mentioned above, if hyperperfusion occurs immediately after surgery, the OEF should theoretically decrease in response to increased blood flow.

Cerebral Perfusion Pressure

Cerebral perfusion pressure (CBF/CBV) rapidly increased during the acute stage. This rapid increase probably indicated that the vasoparalyzed cerebral vessels were unable to react quickly to reperfusion and thus took in much more blood at a low vascular resistance. Over time, self-regulation works to increase vascular resistance and lower CPP; however, vascular reconstruction after surgery increases CPP. The same phenomenon was seen on the healthy side.[14] Recent perfusion MR imaging studies have also found a decrease in transit time in the treated hemisphere after stent placement. Because an inverse relationship exists between transit time and perfusion pressure, our results support these earlier results.[23,35]

Cerebral perfusion pressure is generally considered to reflect cerebral vascular reserve, but our results demonstrate that this is not necessarily the case. The mean % CBF_{az} increased progressively on the ipsilateral side (Fig. 4), but was slightly higher 3–4 months postoperatively than before CAS. The mean % CBF_{az} showed a transient increase in the acute stage (Fig. 6). The reason for unmatched changes in CPP and % CBF_{az} is that although the CPP improved rapidly soon after CAS and then settled afterwards, vascular reserve improved more gradually. In other words, within 1 week of CAS, arterioles that were dilated preoperatively began to contract. Positron emission tomography captured this imbalance at a stage when more CBF was present than necessary—the preparatory stage for hyperperfusion. In hyperperfusion, the close relationship between perfusion pressure and vasodilation reserve breaks down. Over the long-term, however, these parameters are dependent on each other and are higher than in the preoperative period. Changes in CPP and vascular reserve over time after vascular reconstruction therefore differ.

Hyperperfusion syndrome has been reported after CEA and CAS. Patients with hyperperfusion syndrome can experience headaches or convulsions 2–7 days after surgery and sometimes suffer cerebral hemorrhage.[1,7,10,25,29,31] Decreased vascular reserve on preoperative SPECT images has been reported as a predictor of this syndrome.[15,17,27] We found that CPP significantly increased within 1 week of surgery, and that cerebral arterioles could not maintain normal perfusion because of this rapid increase in perfusion pressure. If the vascular walls of arterioles are damaged and permeability is increased, cerebral edema and convulsions can occur. Postoperative infarction or anticoagulant administration also risks cerebral hemorrhage.[12] These findings suggest that the acute stage after CAS is the most dangerous because CPP is abnormally high and vasodilation persists at the arteriolar level. Analysis of preoperative CBV measurements assessed with perfusion MR imaging may help to identify patients at risk for cerebral hyperperfusion after CEA.[6]

In the present study, no patient met the criteria for

postoperative hyperperfusion defined as a CBF increase of ≥ 100%; no laterality of preoperative CPP was present. We believe, however, that a marked decrease in preoperative CPP is a potential risk factor for cerebral hyperperfusion because the value of CPP is strongly associated with the value of CBV.

Study Limitations

Carotid artery stenting is indicated for ICA stenosis > 70%. Because CAS is mainly performed to prevent artery-to-artery embolism, the number of patients with severely decreased CBF was low in the present study. Only 1 patient with misery perfusion displayed an OEF ≥ 0.52, while the rate of CBF_{az} was ≤ 10% in only 2 patients (reduced vascular reserve). From the perspective of cerebral circulation and metabolism, little change was seen in OEF or $CMRO_2$ because there were few patients with severely decreased CBF and metabolism preoperatively. Furthermore, there were only 16 patients included in the study, and 3- to 4-month follow-up data were obtained in only 8 patients.

Conclusions

Repeated PET studies confirmed improvements in CBF, CPP, and oxygen metabolism after CAS. In particular, vascular reserve tended to improve gradually over time, whereas CBF, CPP, and $CMRO_2$ increased rapidly and peaked in the acute stage. Our PET study results support the hypothesis that a large discrepancy between rapidly increased CBF, CPP, and small increases in vascular reserve in the acute stage could cause hyperperfusion syndrome after CAS.

Disclaimer

The authors report no conflict of interest concerning the materials or methods used in this study or the findings specified in this paper.

Acknowledgments

The authors thank Drs. Eku Shimosegawa, Hiroshi Ito, Kumiko Okane, Atsushi Umetsu, Keiichi Ishigame, Ken Okada, and Hatsune Hirota and other staff for their assistance with PET. The authors also thank Hiromi Nishimura for his efforts in computer analysis of the PET data.

Reference

1. Abou-Chebl A, Yadav JS, Reginelli JP, Bajzer C, Bhatt D, Krieger DW, et al: Intracranial hemorrhage and hyperperfusion syndrome following carotid artery stenting: risk factors, prevention, and treatment. **J Am Coll Cardiol 43:**1596–1601, 2004
2. Cikrit DF, Dalsing MC, Harting PS, Burt RW, Lalka SG, Sawchuk AP, et al: Cerebral vascular reactivity assessed with acetazolamide single photon emission computer tomography scans before and after carotid endarterectomy. **Am J Surg 174:**193–197, 1997
3. Derdeyn CP, Cross DT III, Moran CJ, Dacey RG Jr: Reversal of focal misery perfusion after intracranial angioplasty: case report. **Neurosurgery 48:**436–439, 2001
4. Executive Committee for the Asymptomatic Carotid Atherosclerosis Study: endarterectomy for asymptomatic carotid stenosis. **JAMA 273:**1421–1428, 1995
5. Fessler RD, Lanzino G, Guterman LR, Miletich RS, Lopes DK, Hopkins LN, et al: Improved cerebral perfusion after stenting of a petrous carotid stenosis: technical case report. **Neurosurgery 45:**638–642, 1999
6. Fukuda T, Ogasawara K, Kobayashi M, Komoribayashi N, Endo H, Inoue T, et al: Prediction of cerebral hyperperfusion after carotid endarterectomy using cerebral blood volume measured by perfusion-weighted MR imaging compared with single-photon emission CT. **AJNR Am J Neuroradiol 28:**737–742, 2007
7. Friedman JA, Kallmes DF, Wijdicks EF: Thalamic hemorrhage following carotid angioplasty and stenting. **Neuroradiology 46:**399–403, 2004
8. Gibbs JM, Wise RJ, Leenders KL, Jones T: Evaluation of cerebral perfusion reserve in patients with carotid-artery occlusion. **Lancet 1:**310–314, 1984
9. Guimaraens L, Sola MT, Matali A, Arbelaez A, Delgado M, Soler L, et al: Carotid angioplasty with cerebral protection and stenting: report of 164 patients (194 carotid percutaneous transluminal angioplasties). **Cerebrovasc Dis 13:**114–119, 2002
10. Hartmann M, Weber R, Zoubaa S, Schranz C, Knauth M: Fatal subarachnoid hemorrhage after carotid stenting. **J Neuroradiol 31:**63–66, 2004
11. Heiss WD, Herholz K, Jacobs A, Duncan D, Bauer B, Huber M, et al: Increased amino-acid uptake in acute reversible focal ischemia. **J Cereb Blood Flow Metab 13 (1 Suppl):**S564, 1993 (Abstract)
12. Henderson RD, Phan TG, Piepgras DG, Wijdicks EF: Mechanisms of intracerebral hemorrhage after carotid endarterectomy. **J Neurosurg 95:**964–969, 2001
13. Henry M, Henry I, Klonaris C, Masson I, Hugel M, Tzvetanov K, et al: Benefits of cerebral protection during carotid stenting with the PercuSurge GuardWire system: midterm results. **J Endovasc Ther 9:**1–13, 2002
14. Hino A, Tenjin H, Horikawa Y, Fujimoto M, Imahori Y: Hemodynamic and metabolic changes after carotid endarterectomy in patients with high-degree carotid artery stenosis. **J Stroke Cerebrovasc Dis 14:**234–238, 2005
15. Hosoda K, Kawaguchi T, Shibata Y, Kamei M, Kidoguchi K, Koyama J, et al: Cerebral vasoreactivity and internal carotid artery flow help to identify patients at risk for hyperperfusion after carotid endarterectomy. **Stroke 32:**1567–1573, 2001
16. Hosoda K, Fujita S, Kawaguchi T, Shose Y, Shibata Y, Tamaki N, et al: Influence of degree of carotid artery stenosis and collateral pathways and effect of carotid endarterectomy on cerebral vasoreactivity. **Neurosurgery 42:**988–994, 1998
17. Kaku Y, Yoshimura S, Kokuzawa J: Factors predictive of cerebral hyperperfusion after carotid angioplasty and stent placement. **AJNR Am J Neuroradiol 25:**1403–1408, 2004
18. Kanno I, Iida H, Miura S, Murakami M, Takahashi K, Uemura K, et al: A system for cerebral blood flow measurement using an $H_2{}^{15}O$ autoradiographic method and positron emission tomography. **J Cereb Blood Flow Metab 7:**143–153, 1987
19. Kashiwazaki D, Kuroda S, Ushikoshi S, Shichinohe H, Ishikawa T, Asano T, et al: [Normalization of cerebral hemodynamics and metabolism after carotid stenting in patients unfit for major surgery.] **No Shinkei Geka 31:**1315–1320, 2003 (Jpn)
20. Ko NU, Achrol AS, Chopra M, Saha M, Gupta D, Smith WS, et al: Cerebral blood flow changes after endovascular treatment of cerebrovascular stenoses. **AJNR Am J Neuroradiol 26:**538–542, 2005
21. Marchal G, Furlan M, Beaudouin V, Rioux P, Hauttement JL, Serrati C, et al: Early spontaneous hyperperfusion after stroke, a marker of favourable tissue outcome? **Brain 119:**409–419, 1996
22. Marchal G, Young AR, Baron JC: Early postischemic hyper-

perfusion: pathophysiologic insights from positron emission tomography. **J Cereb Blood Flow Metab 19:**467–482, 1999
23. Martin AJ, Saloner DA, Roberts TP, Roberts H, Weber OM, Dillon W, et al: Carotid stent delivery in an XMR suite: immediate assessment of the physiologic impact of extracranial revascularization. **AJNR Am J Neuroradiol 26:**531–537, 2005
24. Mas JL, Chatellier G, Bevssen B, Branchereau A, Moulin T, Becquemin JP, et al: Endarterectomy versus stenting in patients with symptomatic severe carotid stenosis. **N Engl J Med 355:**1660–1671, 2006
25. McCabe DJH, Brown MM, Clifton A: Fatal cerebral reperfusion hemorrhage after carotid stenting. **Stroke 30:**2483–2486, 1999
26. North American Symptomatic Carotid Endarterectomy Trial Collaborators: Beneficial effect of carotid endarterectomy in symptomatic patients with high grade carotid stenosis. **N Engl J Med 325:**445–453, 1991
27. Ogasawara K, Yukawa H, Kobayashi M, Mikami C, Konno H, Terasaki K, et al: Prediction and monitoring of cerebral hyperperfusion after carotid endarterectomy by using single-photon emission computerized tomography scanning. **J Neurosurg 99:**504–510, 2003
28. Ohki T, Veith FJ, Grenell S, Lipsitz EC, Gargiulo N, McKay J, et al: Initial experience with cerebral protection devices to prevent embolization during carotid artery stenting. **J Vasc Surg 36:**1175–1185, 2002
29. Penn AA, Schomer DF, Steinberg GK: Imaging studies of cerebral hyperperfusion after carotid endarterectomy, case report. **J Neurosurg 83:**133–137, 1995
30. Pulsinelli W: Pathophysiology of acute ischaemic stroke. **Lancet 339:**533–536, 1992
31. Shinno K, Ueda S, Uno M, Nishitani K, Nagahiro S, Harada M: [Hyperperfusion syndrome following carotid endarterectomy: evaluation using diffusion-weighted magnetic resonance imaging: case report.] **Neurol Med Chir (Tokyo) 38:**557–561, 1998 (Jpn)
32. Stoll G, Jander S, Schroeter M: Inflammation and glial responses in ischemic brain lesions. **Prog Neurobiol 56:**149–171, 1998
33. Uchiyama N, Kida S, Watanabe T, Yamashita J, Matsui O: Improved cerebral perfusion and metabolism after stenting for basilar artery stenosis: technical case report. **Neurosurgery 48:**1386–1392, 2001
34. Uno M, Harada M, Nagahiro S: Quantitative evaluation of cerebral metabolites and cerebral blood flow in patients with carotid stenosis. **Neurol Res 23:**573–580, 2001
35. Wilkinson ID, Griffiths PD, Hoggard N, Cleveland TJ, Gaines PA, Macdonald S, et al: Short-term changes in cerebral microhemodynamics after carotid stenting. **AJNR Am J Neuroradiol 24:**1501–1507, 2003
36. Yadav JS, Wholey MH, Kuntz RE, Fayad P, Katzen BT, Mishkel GJ, et al: Protected carotid-artery stenting versus endarterectomy in high-risk patients. **N Engl J Med 351:**1493–1501, 2004

Manuscript submitted March 15, 2007.
Accepted September 19, 2008.
Please include this information when citing this paper: published online March 20, 2009; DOI: 10.3171/2008.9.17663.
Address correspondence to: Akifumi Suzuki, M.D., Ph.D., 6-10, Senshu-Kubota-machi, Akita 010-0874, Japan. email: akifumi@akita-noken.go.jp.

Ann Nucl Med (2009) 23:163–171
DOI 10.1007/s12149-008-0226-0

ORIGINAL ARTICLE

Improvement of likelihood estimation in Logan graphical analysis using maximum a posteriori for neuroreceptor PET imaging

Miho Shidahara · Chie Seki · Mika Naganawa
Muneyuki Sakata · Masatomo Ishikawa · Hiroshi Ito
Iwao Kanno · Kiichi Ishiwata · Yuichi Kimura

Received: 21 May 2008 / Accepted: 16 November 2008

Abstract
Objective To reduce variance of the total volume of distribution (V_T) image, we improved likelihood estimation in graphical analysis (LEGA) for dynamic positron emission tomography (PET) images using maximum a posteriori (MAP).
Methods In our proposed MAP estimation in graphical analysis (MEGA), a set of time–activity curves (TACs) was formed with V_T varying in physiological range as a template, and then the most similar TAC was sought out for a given measured TAC in a feature space. In simulation, MEGA was compared with other three methods, Logan graphical analysis (GA), multilinear analysis (MA1), and LEGA using 500 noisy TACs, under each of seven physiological conditions (from 9.9 to 61.5 of V_T). PET studies of [^{11}C]SA4503 were performed in three healthy volunteers. In clinical studies, the V_T images estimated from MEGA were compared with region of interest (ROI) estimates from a nonlinear least square (NLS) fitting over four brain regions.
Results In the simulation study, the estimated V_T by GA had a large underestimation ($y = 0.27x + 8.72$, $r^2 = 0.87$). Applying the other methods (MA1, LEGA, and MEGA), these noise-induced biases were improved ($y = 0.80x + 4.04$, $r^2 = 0.98$; $y = 0.85x + 3.05$, $r^2 = 0.99$; $y = 0.96x + 1.21$, $r^2 = 0.99$, respectively). MA1 and LEGA produced increased variance of the estimated V_T in clinical studies. However, MEGA improved signal-to-noise ratio (SNR) in V_T images with linear correlations between ROI estimates with NLS ($y = 0.87x + 5.1$, $r^2 = 0.96$).
Conclusions MEGA was validated as an alternative strategy of LEGA to improve estimates of V_T in clinical PET imaging.

Keywords Positron emission tomography · MAP-based estimation algorithm in graphical analysis · Logan graphical analysis · Kinetic analysis

M. Shidahara (✉) · C. Seki · M. Naganawa · H. Ito · I. Kanno · Y. Kimura
Molecular Imaging Center, National Institute of Radiological Sciences, 4-9-1 Anagawa, Inage-ku, Chiba, 263-8555, Japan
e-mail: sidahara@nirs.go.jp

M. Sakata · M. Ishikawa · K. Ishiwata · Y. Kimura
Positron Medical Center, Tokyo Metropolitan Institute of Gerontology, Tokyo, Japan

M. Ishikawa
Department of Psychiatry, Chiba University Graduate School of Medicine, Chiba, Japan

Introduction

Logan graphical analysis (GA) was originally proposed to quantify the total volume of distribution (V_T) (ml/cm^3) for reversibly binding neuroreceptor tracers [1]. V_T is equivalent to the slope in GA and is a linear relationship between two ratios: the integrated time–activity curve (TAC) in arterial plasma (pTAC) and the TAC in tissue (tTAC). The advantages of using GA are the rapid determination of V_T and its low variance. However, it suffers from noise-induced bias. Because tTAC is included in the independent variable of GA, the slope is underestimated in any line estimation [2, 3]. Slifstein et al. [3] reported that such underestimation depends on the magnitude of both the noise and the true V_T. Therefore, the underestimation is severe, especially in voxel-based parametric imaging or in calculation of parameters in regions with high V_T.

Recently, several approaches to overcome this problem have been proposed. These methods include

pre- or post-smoothing of images [4–6], GA together with principal component analysis [7], multilinear analysis (MA1) [8], and likelihood estimation in graphical analysis (LEGA) [9]. Although the approaches using smoothing are effective, they are not direct improvements to GA. GA together principal component analysis was proposed to improve linear estimation. However, it still suffered from bias in the estimates [7]. On the other hand, MA1 [8] and LEGA [9] succeeded in reducing the bias. MA1 is the same linear estimation method as GA. To suppress noise-induced bias, the term for tTAC is replaced with its integral so that the noise in tTAC affects the estimates less than does GA [8]. On the other hand, the number of independent variables is larger than with GA. Thus, the variance in the estimates of MA1 is greater than with GA. In LEGA, the relationship between pTAC and tTAC was introduced based on GA that contained V_T as a parameter. V_T was then estimated using a nonlinear optimization algorithm [9]. Even though LEGA overcomes noise-induced bias, both computing time and variance in the estimates are increased. If the noise level is increased, variances in both MA1 and LEGA remain. Therefore, if variance can be suppressed, the signal-to-noise ratio (SNR) of V_T images is improved and clinically acceptable V_T images can be generated.

To reduce both estimation variance and the noise-induced bias in the estimated V_T, we introduced a maximum a posteriori (MAP) approach into the estimation process in LEGA. This MAP-based parametric imaging improved robustness for noise interference and shortened the calculation time for parametric imaging using [^{18}F]-fluorodeoxyglucose ([^{18}F]FDG) [10]. We carried out simulation studies to determine the details of the proposed MAP-based estimation algorithm in graphical analysis (MEGA), and to evaluate its reliability compared with GA, MA1, and LEGA. Here we discuss MEGA-based V_T images using dynamic PET data for [^{11}C]-labeled 1-(3,4-dimethoxymethyl)-4-(3-phenylpropyl) piperazine hydrochloride ([^{11}C]SA4503) [11–13], which is a selective ligand for the sigma$_1$ receptor in the brain.

Materials and methods

Kinetic analysis

Logan graphical analysis (GA)

GA provides V_T using pTAC and tTAC information only after reaching equilibrium [1]. V_T is estimated from the following equation:

$$\frac{\int_0^t C(u)du}{C(t)} = V_T \frac{\int_0^t C_p(u)du}{C(t)} + b \quad t \geq t^*, \tag{1}$$

where C_p is the radioactivity concentration in the metabolite corrected plasma and C is the radioactivity concentration in the tissue. Because V_T and b become constants only after equilibration time t^*, V_T, and b are estimated as a slope and an intercept, respectively, using the frames of $t \geq t^*$.

MA1 method

Equation 1 can be rearranged to give Eq. 2 and reduce noise-induced bias [8] thus:

$$C(t) = \beta_1 \int_0^t C_p(u)du + \beta_2 \int_0^t C(u)du \quad t \geq t^*, \tag{2}$$

$\beta_1 = -V_T/b$ and $\beta_2 = 1/b$ are estimated by linear regression analysis for $t \geq t^*$, and V_T is calculated from $-\beta_1/\beta_2$.

LEGA

According to Ogden et al. [9], Eq. (1) can be rearranged using the trapezoidal approximation to produce the recursive relationship as follows:

$$C^*(t_i) = \frac{\int_0^{t_{i-1}+\frac{\Delta t_{i-1}}{2}} C^*(u)du + \frac{1}{8}C^*(t_{i-1})\Delta t_i - V_T \int_0^{t_i} C_p(u)du}{b - \frac{3}{8}\Delta t_i}$$
$$t_i \geq t_k, \tag{3}$$

where C^* indicates the estimated TAC, and t_i is the mid-scan time, Δt_i is the scan duration of ith frame. GA is available after the time at t_k, where k is the frame number. t_k has the same meaning as t^* in Eq. 1. The maximum likelihood estimate is obtained by minimizing a sum of squared residuals between $C^*(t_i)$ and a measured tTAC of $C(t)$ with respect to V_T and b. The estimated result of GA was set to the initial value for LEGA.

MEGA

In general, MAP estimation calculates a parameter s while maximization of $P(D|s)P(s)$, where $P(D|s)$ and $P(s)$ are likelihood of datasets D and prior probability of s, respectively. In MEGA, the Mahalanobis distance in a feature space was utilized for the likelihood term in LEGA, and a uniform distribution between given lower and upper bounds was applied for the prior.

Practically, a set of noise-free tTACs is formed before parameter estimation as a template with a priori knowledge of the kinetics of the administered radiopharmaceutical, and then the most similar tTAC is sought out for a given measured tTAC. The corresponding kinetic parameter for the tTAC in the template is adopted for an estimation [10]. We extended these ideas to LEGA and the following procedures were included in MEGA.

1. A set of (V_T, b) was defined discretely within a physiologically feasible range.
2. Sets of $C(t_{k-1})$ and $\int_0^{t_{k-1}} C(t)dt$ were specified by measured tTACs.
3. Applying Eq. 3, a set of corresponding noise-free tTACs was computed using (V_T, b), $C(t_{k-1})$, $\int_0^{t_{k-1}} C(t)dt$ and a measured arterial input function $C_P(t)$.
4. The covariance at a noise-free tTAC in step 3 was calculated using noisy tTACs.
5. The most similar tTAC to the given measured tTAC was searched for among the prepared noise-free tTACs in step 3 using the covariance in step 4. Finally the corresponding V_T for the tTAC was adopted for an estimation of V_T.

Estimation in this approach is performed in a feature surface, which is a mathematical representation of a set of shapes of the generated tTACs. To define a feature surface, a single tTAC is considered as a vector in L-dimensional space where L is the number of frames used for GA and $L = N - k + 1$ (Fig. 1a). N is the total number of frames.

$$\mathbf{C} \equiv [C(t_k), \ldots, C(t_N)]^T \quad (4)$$

Then, all the generated tTACs are composed as a matrix $\mathbf{C}_A$:

$$\mathbf{C}_A \equiv [C_1, \ldots, C_l] \quad (5)$$

where l is the number of tTACs. After applying principal component analysis to $\mathbf{C}_A$, the dimensionality of the data was reduced from L to 2. We defined the projected $\mathbf{C}_A$ into two-dimensional space as a feature surface (Fig. 1b). Note that a priori tTACs were derived from varying V_T values ranging between 0 and 80 with a step size of 1, and from b values between −200 and 0 with a step of −10 for values smaller than −40, otherwise with a step of −1 in the present study and the feature surface is defined by $C(t_{k-1})$ and $\int_0^{t_{k-1}} C(t)dt$ as well as V_T and b (Eq. 3) at step 2. $C(t_{k-1})$ and $\int_0^{t_{k-1}} C(t)dt$ are given as a measured tTAC. To simplify MEGA, the feature surfaces were composed for a set of $C(t_{k-1})$ and $\int_0^{t_{k-1}} C(t)dt$, which was specified considering a given tTAC. In the estimation, the feature surface having the nearest $C(t_{k-1})$ and $\int_0^{t_{k-1}} C(t)dt$ of a given tTAC was selected. Then the most similar tTAC in the template to a given tTAC was searched for.

The noise in a measured tTAC is taken into consideration as described below. Assume that the noise-free tTAC with a combination of (V_T, b) is projected onto the point $P(V_T, b)$ in a feature surface. The noise changes the shape of tTAC, and causes fluctuation of the projection

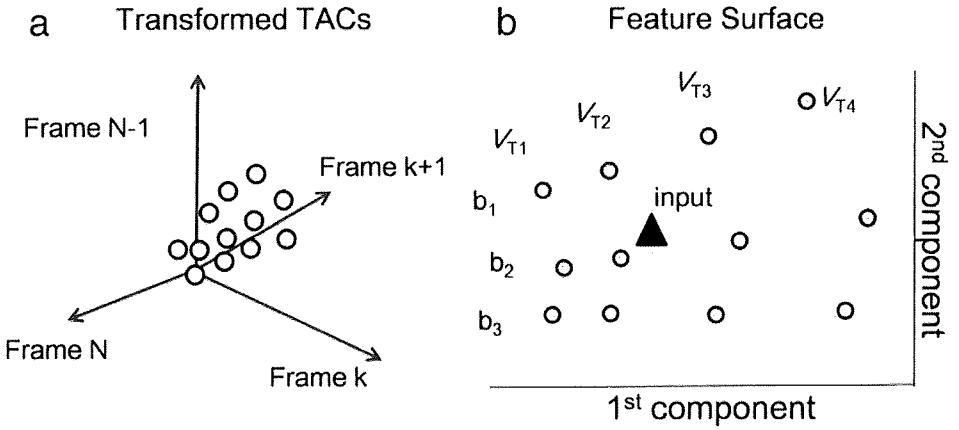

Fig. 1 Illustration of a feature surface in MEGA. **a** First, noise-free tTAC, $C(t_i)$ ($i = k, \ldots, N$), is plotted (*open circle*) along the axes of frames. The number of its dimensions is L ($= N - k + 1$). **b** Applying principal component analysis, the L-dimensional space is decomposed into two components. To estimate V_T, the Mahalanobis distance between the point corresponding to the measured data (*filled triangle*) and each noise-free point with known V_T (*open circle*) is calculated, and then the nearest point is selected as estimate V_T

around P. To obtain the statistical properties of the fluctuation under the assumption of Gaussianity in the noise propagation, the covariance $\Sigma(V_T, b)$ at each noise-free point $P(V_T, b)$ was calculated using noisy tTACs [10] at step 4. Gaussian noise was added to simulate a realistic measurement situation using the following equation [8]:

$$C_{\text{Noise}}(t_i) = \tilde{C}(t_i) + R\sigma_i, \quad \sigma_i = A\frac{\sqrt{\tilde{C}(t_i)e^{(\lambda t_i)}}}{\Delta t_i} \tag{6}$$

where $C_{\text{Noise}}(t_i)$ is noise-added tTAC, $\tilde{C}(t_i)$ is the noise-free tTAC, R is a normal distribution random number (its mean and variance are 0 and 1, respectively), A is the scale factor that controls the level of noise, λ is the radioisotope decay constant, and Δt_i is the scan duration. Noisy tTACs for the covariance $\Sigma(V_T, b)$ were generated where A in Eq. 6 was set at 40 to simulate voxel-based tTACs.

Finally, to determine estimates of b and V_T, the Mahalanobis distance between the point of measured data P_{obs} and each noise-free point $P(V_T, b)$ was calculated with covariance $\Sigma(V_T, b)$, and then, the nearest point was selected achieving the smallest Mahalanobis distances and the corresponding V_T and b values were adopted as the estimates as follows

$$(V_T, b) = \arg\min_{V_T, b}\left[(P_{\text{obs}} - P(V_T, b))^T \sum (V_T, b)^{-1}(P_{\text{obs}} - P(V_T, b))\right]. \tag{7}$$

Simulation study

A simulation study was performed to validate MEGA using each 500 realizations of noisy tTACs in six conditions in which V_T was set to 20.5 ml/cm^3, 21.4 ml/cm^3, 29.6 ml/cm^3, 41.5 ml/cm^3, 42.9 ml/cm^3, and 61.5 ml/cm^3. These covered normal physiological changes in the [^{11}C]SA4503 values as measured in clinical studies [11, 13]. The noise levels of these simulations mimicked both noises in the region of interest (ROI) (A = 5 in Eq. 6) and in each voxel (A = 40). Plasma input function for the simulation and an example of a simulated TAC are shown in Fig. 2. At first, sampling interval for simulated TAC was a second and then averaged by each frame. An integral of simulated tTAC was implemented with the sum of $(C(t_k) \times \Delta t_k)$. Kinetic parameters were estimated based on the two-tissue three-compartment model using nonlinear least square (NLS) fitting of ROIs in the frontal cortex, caudate, and cerebellum at baseline [the number of subjects (n) = 13] and under fluvoxamine-loading (n = 3) conditions [11]. Furthermore, the case of k_3 equal to 0.110 was prepended to investigate the performance of MEGA in the case of a small V_T value (9.9). Detailed conditions of these NLS fittings were described by Sakata et al. [13] and details of kinetic parameters are listed in Table 1. The true V_T (V_T^{true}) was computed as $(K_1/k_2)(1 + k_3/k_4)$.

Estimations of V_T for these conditions with GA (V_T^{GA}), with MA1 (V_T^{MA1}), with LEGA (V_T^{LEGA}) and with the proposed MEGA (V_T^{MEGA}) were compared against (V_T^{true}). The time interval for all analyses was fixed from 30 min to 90 min [13].

In this simulation, we handled 3500 TACs (500 × 7) in a group. For MEGA, the histograms of $C(t_{k-1})$ and $\int_0^{t_{k-1}} C(t)dt$ for the feature surfaces were each divided into seven bins and then the combinations of divided $C(t_{k-1})$ and $\int_0^{t_{k-1}} C(t)dt$ were generated.

Furthermore, estimated V_T by MEGA with three combinations of parameters (number of point for

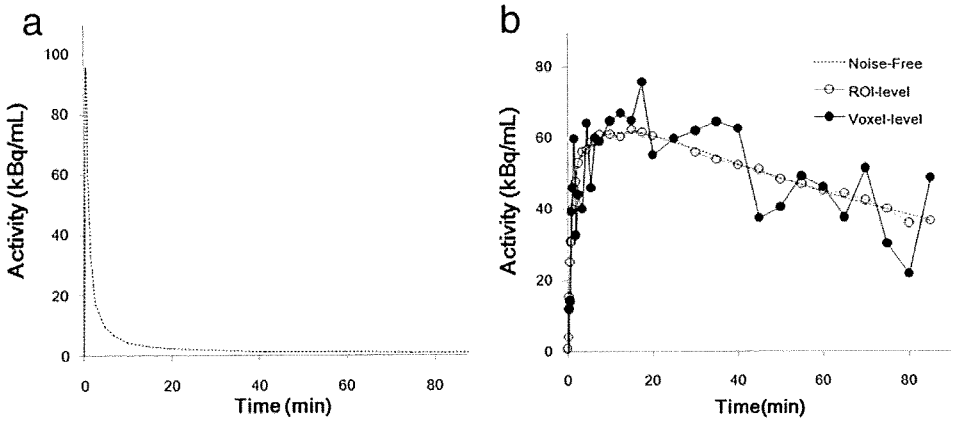

Fig. 2a Metabolite-corrected plasma TAC used as an input function for the simulation. **b** Example of simulated time–activity curve (10 s × 6 frames, 30 s × 3 frames, 60 s × 5 frames, 150 s × 5 frames and 300 s × 14 frames) providing a V_T = 20.5 for [^{11}C]SA4503

Table 1 Kinetic parameters for the simulation study of [^{11}C]SA4503

Regions	V_T (ml/cm^3)	K_1 [ml/(cm^3/min)]	k_2 (min^{-1})	k_3 (min^{-1})	k_4 (min^{-1})
–	9.9	0.550	0.158	0.110	0.0597
Caudate (L)	20.5	0.550	0.158	0.292	0.0597
Frontal cortex (L)	21.4	0.522	0.178	0.288	0.0457
Cerebellum (L)	29.6	0.590	0.204	0.332	0.0360
Caudate (B)	41.5	0.562	0.207	0.401	0.0281
Frontal cortex (B)	43.0	0.516	0.195	0.414	0.0272
Cerebellum (B)	61.5	0.530	0.200	0.490	0.0221

L and *B* indicate loading and baseline conditions

covariance and maximum value of V_T and minimum value of b) were compared under voxel-level noise.

Clinical study

Carbon-11-labeled SA4503 is the radioligand for sigma$_1$ receptors, which are related to neurological and psychiatric neurophysiologies [14]; its kinetic model follows a two-tissue three-compartment [13]. The binding potential of [^{11}C]SA4503 in ROIs has been used for occupancy study with selective serotonin reuptake inhibitor (SSRI) because some SSRIs possess high to moderate affinities for sigma$_1$ receptors [11, 15]. Instead of no reference regions, it is reported that V_T can be an alternative to the binding potential for [^{11}C]SA4503 [16]. Therefore, the quantification of V_T imaging in [^{11}C]SA4503 study is important.

PET studies were performed in three normal male volunteers (age 41 years–42 years) at baseline and under fluvoxamine-loading conditions using SET-2400 PET scanner (Shimadzu, Kyoto, Japan) at the Positron Medical Center, Tokyo Metropolitan Institute of Gerontology. First, a 90-min dynamic PET scan in 2D mode (10 s × 6 frames, 30 s × 3 frames, 60 s × 5 frames, 150 s × 5 frames, and 300 s × 14 frames) was performed, then a second scan was conducted 4.0 h or 4.5 h after the oral administration of 200 mg fluvoxamine (Luvox: Astellas, Tokyo, Japan), which is an SSRI but has a moderate affinity for sigma$_1$ receptors. A transmission scan was performed with a rotating ^{68}Ga/^{68}Ge rod source for 5 min for attenuation correction before the administration of the tracer. After the bolus injection, total 26 blood samples were manually taken and their plasma concentration of radioactivity was measured ten times during the initial 2 min, twice during the next 30 s, and then 12 times until the end of the scan. Five samples collected at 3 min, 10 min, 20 min, 30 min and 40 min were further processed by high performance liquid chromatography for metabolite analysis. The dynamic image (128 × 128 × 50 pixels with 2 mm × 2 mm × 3.125 mm) was reconstructed with a filtered back-projection algorithm using a Butterworth filter (1.25 cycles/cm, order 2). The Ethics Committee of the Tokyo Metropolitan Institute of Gerontology approved the study protocols, and informed consent was given by all subjects.

Parametric images of V_T for three volunteers at the baseline and loading conditions were formed using voxel-based GA, MA1, LEGA, and MEGA analyses. These results were compared with ordinary ROI averaged estimates. ROIs were defined over four regions: the frontal cortex, parietal cortex, caudate and cerebellum [11, 13].

To execute MEGA, the combinations of divided $C(t_{k-1})$ and $\int_0^{t_{k-1}} C(t)dt$ for the feature surfaces were divided into 20 and 10 bins of histograms, respectively.

Results

Simulation study

We first studied the dependency of the number of noisy tTAC at a projected point in a feature surface for covariance and the range of V_T and b. By varying these conditions, we were able to obtain similar estimation results as shown in Fig. 3. Therefore, to speed up the computing time, we selected the present conditions (five tTACs for covariance, maximum of $V_T = 80$ and minimum of $b = -200$).

Figure 4 shows the comparison of estimated V_T at ROI-noise level (*a*) and voxel-noise level (*b*) by the four methods against true V_T. For a small noise level, there were no differences among the four methods (Fig. 4a). V_T^{GA} gave us the most stable V_T estimates, but they were largely underestimated against the true values, especially at a voxel noise level ($y = 0.27x + 8.72$, $r^2 = 0.87$). The tendency of this underestimation was not varied even though t^* was later than 30 min (e.g., 40 min or 50 min) for GA (data not shown). All advanced algorithms of

MA1, LEGA, and MEGA produced better estimates ($y = 0.80x + 4.04$; $r^2 = 0.98$, $y = 0.85x + 3.05$, $r^2 = 0.99$, $y = 0.96x + 1.21$, $r^2 = 0.99$, respectively; Fig. 4b). However, the variance in estimation of MEGA was the smallest of the three algorithms. At $V_T = 61.5$ in Fig. 4b, the upper quartile ranges of V_T^{MA1} and V_T^{LEGA} were 2.2 and 3.4 times larger than that of V_T^{MECA}, respectively.

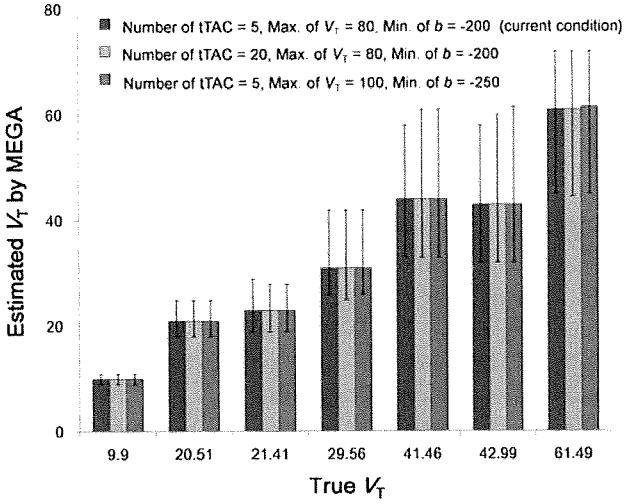

Fig. 3 Comparison of estimated V_T by MEGA with three combinations of parameters (number of tTAC for covariance and maximum value of V_T and minimum value of b) in simulation study (voxel-level noise). The estimates are plotted with respect to the true values. The *lower*, *middle*, and *upper edges* denote the 25th, 50th, and 75th percentiles

Clinical studies

Figure 5 demonstrates a comparison of V_T images of [^{11}C]SA4503 at baseline and fluvoxamine-loading conditions for the four methods. Because Fluvoxamine possesses high to moderate affinities for sigma$_1$ receptors [11], V_T images at fluvoxamine-loading were decreased compared with those at baseline. The V_T^{GA} values estimated by GA were severely underestimated compared with the other three methods. MA1 and LEGA improved these underestimations, but there were many unsuccessful estimates in V_T^{MA1} and V_T^{LEGA} at both baseline and loading conditions. On the other hand, an improvement in the SNR for V_T^{MEGA} was observed visually.

Figure 6 shows a comparison of the V_T^{MEGA} in ROIs with the estimated V_T using ROI-averaged tTAC and NLS. The median of V_T^{MEGA} in ROIs was linearly correlated with the ROI-based estimates of V_T with NLS ($y = 0.87x + 5.08$, $r^2 = 0.96$). The similar linearity ($y = 0.85x - 26.91$, $r^2 = 0.94$) was observed in intercept b by comparing the median of b^{MEGA} in ROIs and the ROI-based f b^{NLS}, calculated by estimated k parameters [3].

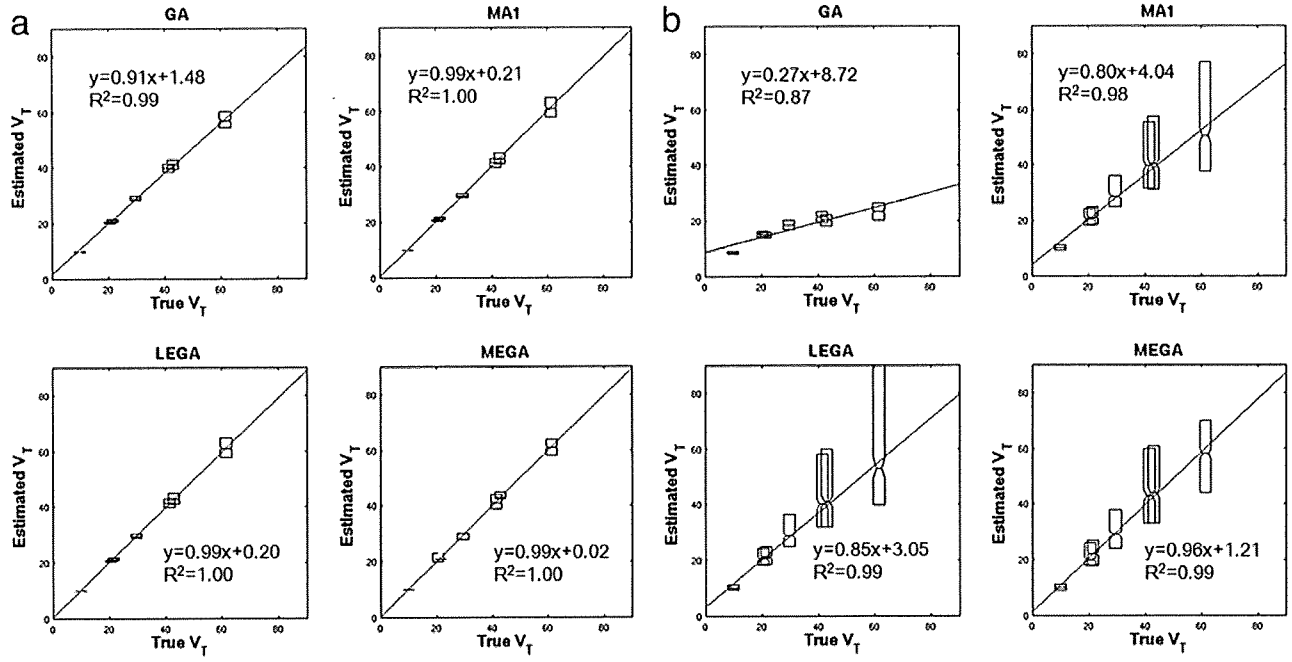

Fig. 4 Comparison of the total volume of distribution (V_T) estimated by GA, MA1, LEGA and MEGA from noisy TACs (n = 500) corresponding to a noise level in the region of interest (ROI) (**a**) and in a voxel (**b**). The estimates are plotted as box plots with respect to the true values. The *lower*, *middle*, and *upper edges* denote the 25th, 50th and 75th percentiles, respectively. Regression lines between the true and the median of the estimates are superimposed

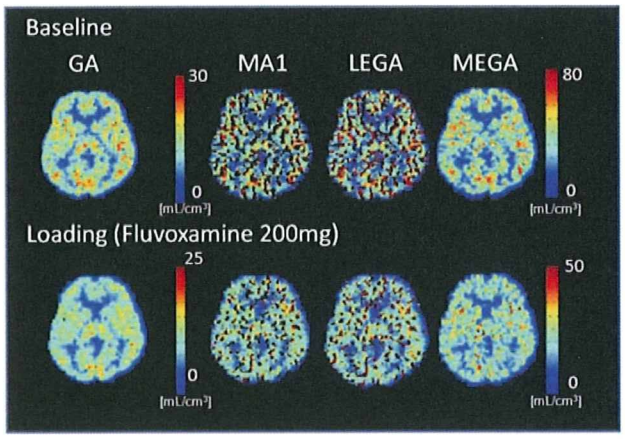

Fig. 5 Comparison of the total volume of distribution images of [^{11}C]SA4503-PET estimated by GA, MA1, MEGA and LEGA. *Top* baseline condition, *bottom* fluvoxamine-loading condition

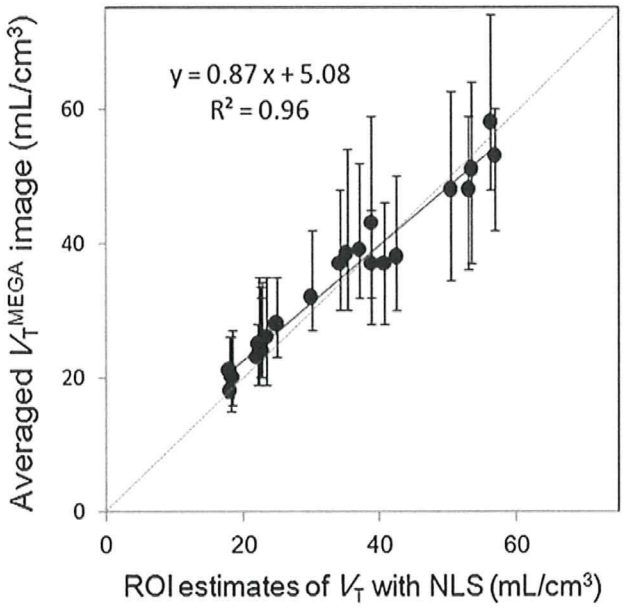

Fig. 6 Comparison of ROI-based estimates of total volume of distribution (V_T) based on a two-tissue three-compartment model using nonlinear least square and median of V_T images generated by MEGA. The *lower* and *upper edges* denote the 25th and 75th percentiles, respectively. The regression line between ROI estimates of V_T with NLS and the medians of estimates with MEGA is superimposed

Discussion

In the present study, we have proposed this MAP-based estimation algorithm in GA, which compares the shape of measured and prepared tTACs in a feature surface and estimates V_T using Mahalanobis distance. MEGA was applied to simulation and clinical data sets for its evaluation.

In the simulation study, V_T^{GA} was underestimated as the noise increased (Fig. 4). The three other methods, MA1, LEGA, and MEGA, suppressed the noise-induced bias of V_T compared with GA. The differences among MA1, LEGA and MEGA were fluctuations in the estimates of V_T. MA1 and LEGA provided large quartile ranges of estimates at high V_T values, but that produced by MEGA was smaller (Fig. 4b). In MEGA, a priori knowledge of the investigated ligand was incorporated into the estimation process, such as the range of physiologically feasible V_T values, and this gave reliable results. Thus, the median of V_T^{MEGA} was equivalent to 61.5 of V_T^{true} (Fig. 4b). In the clinical studies, an improvement in the SNR for V_T^{MEGA} was observed visually compared with those in V_T^{MAI} and V_T^{LEGA} images (Fig. 5). This observation was consistent with the simulation study. The median of V_T^{MEGA} values in ROIs were correlated linearly with the ROI-based estimates of V_T with NLS (Fig. 6).

Considering both the simulated and clinical results, MEGA was effective for improving the image quality of estimated parametric images, especially in ligands with high V_T values. Therefore, V_T^{MEGA} imaging of [^{11}C]SA4503 will have an important role in clinical investigations.

In the simulation, good coincidence of V_T^{MEGA} with the true V_T was achieved over a wide range of V_T values. For such ligands that have a reference region, V_T is distributed widely because the V_T is small in a given reference region. A preferable outcome in neuroreceptor imaging is BP_{ND} defined as the ratio of k_3 and k_4, and this can be derived as the ratio of two V_T values in a target tissue and a reference region [17]. Therefore, MEGA is applicable to receptor imaging with a reference region.

Two practical issues of computational time and appropriate statistic are considered.

Originally, the MAP-based estimation approach proposed by Kimura et al. [10] was based on only one feature surface with assumed various kinetic parameters. In other words, once one builds a feature surface with these assumed kinetic parameters, fast computing is feasible for parametric imaging, similar to a lookup table technique. On the other hand, our algorithm requires hundreds of feature surfaces dependent on combinations of measured and clustered $C(t_{k-1})$ and $\int_0^{t_{k-1}} C(t)dt$ of TACs. To avoid reducing accuracy because of wide clustering intervals, we have divided $C(t_{k-1})$ and $\int_0^{t_{k-1}} C(t)dt$ of whole individual brain into 200 combinations (20 and 10 bins, respectively). Therefore, our present algorithm needs much more computing time than a previous approach [10]. Additionally, detail optimization (e.g., for combinations of clustered $C(t_{k-1})$ and $\int_0^{t_{k-1}} C(t)dt$ or

upper/lower limit for V_T) will be necessary. So further investigations will be required. However, current computing time is not a problem for practical use (about 1 h for a whole brain calculation using 3.2 GHz CPU and 4 GB memory on Linux machine). As shown in Figs. 4 and 6, a median of V_T was used because the two distances from the median to the 25th and 75th percentiles were not equal in MEGA. In other words, MEGA's estimates have a non-Gaussian property. This may be caused by the characteristics of the feature surface, which was heavily distorted as shown in a previous study [10]. Thus, the amount of variance in estimates may tend to be asymmetric, giving a non-Gaussian property.

A priori information is important for the accuracy in MEGA. The range of V_T values for [^{11}C]SA4503 in the major cortex is 20 ml/cm^3–60 ml/cm^3 [11, 13]. Therefore, we defined a sampling interval for V_T as 1. If the target ligand provides a small V_T (~10 ml/cm^3), the sampling interval should be smaller than 1. As with V_T, in the case of an intercept b close to zero, the sampling interval of b for MEGA should be smaller. Therefore, we set separate intervals of b for $b > -40$ and $b \leq -40$. Without such adjustment, MEGA produces poor estimates (data not shown). Using an averaged V_T with a weighted Mahalanobis distance might produce estimations that are more accurate and suppress the error caused by rough intervals; this will be investigated further. Concerning about the feature surface, the same tTACs ($t \geq t_k$) with different V_T will be projected into the same point in that space. In such a case, MEGA might provide poor estimates of V_T values. The one redeeming feature is that a prepared TAC requires $C(t_{k-1})$ and $\int_0^{t_{k-1}} C(t)dt$ of measured input data, because these conditions reduce the probability of overlapping several projected points in the feature surface.

For noise suppression in MEGA, three factors are mainly involved: (1) definition of upper and lower limits in V_T, (2) noise-model for estimation process, and (3) decimation of the dimension in the feature spaces. As shown in Fig. 3, these upper and lower limit values did not affect estimated V_T by MEGA, so we think that this factor (1) is not major. MEGA without any noise models increases bias compared with proposed MEGA (data not shown). This indicates that the effect of decimated feature space seems not for reduction of bias in V_T estimates, even though decimated feature space has been expected to make the estimation process more robust than conventional TAC estimation, and still noise model is necessary. The combination of decimation of feature space and noise modeling seems important for MEGA.

In our proposed method, PCA is a key processing step for decimation of the dimension in the feature space. Recently, Joshi et al. [18] proposed temporal denoising technique using PCA as a pre-processing of reference Logan Plot. A measured TAC is denoised using a sum of a few principal components defined by all TACs over brain regions. They used PCA for denoising purposes, differing from MEGA, which used PCA as reduction of estimation dimension. PCA could be an important algorithm for parametric imaging.

Conclusions

The new alternative method to likelihood estimation in GA, MEGA, has been proposed and evaluated as a valid strategy to improve V_T estimates. Especially, MEGA may be useful for high V_T imaging.

Acknowledgments This study was supported in part by grants-in-aid for Young Scientists (B) (No. 19700395), for JSPS Fellows (No. 186916), and for Scientific Research (C) (No. 18591373) from the Ministry of Education, Culture, Sports, Science and Technology, Japan. The authors thank the staff of the Positron Medical Center at the Tokyo Metropolitan Institute of Gerontology for the PET measurements.

References

1. Logan J, Fowler JS, Volkow ND, Wolf AP, Dewey SL, Schlyer DJ, et al. Graphical analysis of reversible radioligand binding from time-activity measurements applied to [*N*-11C-methyl]-(−)-cocaine PET studies in human subjects. J Cereb Blood Flow Metab 1990;10:740–7.
2. Carson RE. PET parameter estimation using linear integration methods: bias and variability considerations. In: Uemura K, Lassen NA, Jones T, Kanno I (eds) Quantification of brain function: tracer kinetics and image analysis in brain PET. New York: Excerpta Medica 1993, pp. 499–507.
3. Slifstein M, Laruelle M. Effects of statistical noise on graphic analysis of PET neuroreceptor studies. J Nucl Med 2000;41: 2083–8.
4. Logan J, Fowler JS, Volkow ND, Ding YS, Wang GJ, Alexoff DL. A strategy for removing the bias in the graphical analysis method. J Cereb Blood Flow Metab 2001;21:307–20.
5. Turkheimer FE, Aston JA, Asselin MC, Hinz R. Multi-resolution Bayesian regression in PET dynamic studies using wavelets. Neuroimage 2006;32:111–21.
6. Wen L, Eberl S, Feng D, Cai W, Bai J. Fast and reliable estimation of multiple parametric images using an integrated method for dynamic SPECT. IEEE Trans Med Imaging 2007;26:179–89.
7. Varga J, Szabo Z. Modified regression model for the Logan plot. J Cereb Blood Flow Metab 2002;22:240–4.
8. Ichise M, Toyama H, Innis RB, Carson RE. Strategies to improve neuroreceptor parameter estimation by linear regression analysis. J Cereb Blood Flow Metab 2002;22: 1271–81.
9. Ogden RT. Estimation of kinetic parameters in graphical analysis of PET imaging data. Stat Med 2003;22: 3557–68.

10. Kimura Y, Naganawa M, Yamaguchi J, Takabayashi Y, Uchiyama A, Oda K, et al. MAP-based kinetic analysis for voxel-by-voxel compartment model estimation: detailed imaging of the cerebral glucose metabolism using FDG. Neuroimage 2006;29:1203–11.
11. Ishikawa M, Ishiwata K, Ishii K, Kimura Y, Sakata M, Naganawa M, et al. High occupancy of sigma-1 receptors in the human brain after single oral administration of fluvoxamine: a positron emission tomography study using [11C]SA4503. Biol Psychiatry 2007;62:878–83.
12. Kawamura K, Ishiwata K, Tajima H, Ishii S, Matsuno K, Homma Y, et al. In vivo evaluation of [(11)C]SA4503 as a PET ligand for mapping CNS sigma(1) receptors. Nucl Med Biol 2000;27:255–61.
13. Sakata M, Kimura Y, Naganawa M, Oda K, Ishii K, Chihara K, et al. Mapping of human cerebral sigma1 receptors using positron emission tomography and [11C]SA4503. Neuroimage 2007;35:1–8.
14. Su TP, Hayashi T. Understanding the molecular mechanism of sigma-1 receptors: towards a hypothesis that sigma-1 receptors are intracellular amplifiers for signal transduction. Curr Med Chem 2003;10:2073–80.
15. Narita N, Hashimoto K, Tomitaka S, Minabe Y. Interactions of selective serotonin reuptake inhibitors with subtypes of sigma receptors in rat brain. Eur J Pharmacol 1996;307:117–9.
16. Kimura Y, Naganawa M, Sakata M, Ishikawa M, Mishina M, Oda K, et al. Distribution volume as an alternative to the binding potential for sigma1 receptor imaging. Ann Nucl Med 2007;21:533–5.
17. Innis RB, Cunningham VJ, Delforge J, et al. Consensus nomenclature for in vivo imaging of reversibly binding radioligands. J Cereb Blood Flow Metab 2007;27:1533–9.
18. Joshi A, Fessler JA, Koeppe RA. Improving PET receptor binding estimates from Logan plots using principal component analysis. J Cereb Blood Flow Metab 2008;28:852–65.

動物実験手技集成

監修　寺本　昇

国立循環器病センター　研究所　先進医工学センター　放射線医学部

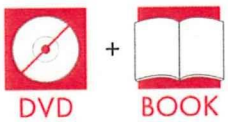

NTS

動物実験手技集成

CONTENTS

監修・解説：

国立循環器病センター　研究所
先進医工学センター　放射線医学部

寺本 昇

（取り扱いのご注意）
●ディスクは両面とも、指紋、汚れ、キズなどをつけないように取り扱ってください。
●ディスクが汚れたときは、メガネふきのようなやわらかい布を軽く水で湿らせ、内側から外側に向かって放射状に軽くふきとってください。レコード用クリーナーや溶剤等は使用しないでください。
●ディスクは両面共、鉛筆、ボールペン、油性ペン等で文字や絵を描いたり、シール等を貼付しないでください。
●ひび割れや変形、または接着剤等で修復されたディスクは危険ですから絶対に使用しないでください。また静電気防止スプレー等の使用は、ひび割れの原因となることがあります。
（保管上のご注意）
●使用後は、必ずプレーヤーから取り出し、DVD専用ケースに納めて、直射日光の当たるところや高温多湿の場所は避けて保管してください。
●ディスクケースの上に重いものを置いたり、落としたりすると、ケースが破損し、ケガをすることがあります。

株式会社 エヌ・ティー・エス
〒113-0034　東京都文京区湯島2-16-16
TEL.03-3814-9151　FAX.03-3814-9152
http://www.nts-book.co.jp/

NTSNM-00004	レンタル禁止	NTSC 日本市場向
片面・一層	モノラル	
COLOR MPEG-2	DOLBY DIGITAL	4:3
複製不能